The Low-Energy Unimolecular Reaction Rate Constants for the Gas Phase, Ni^+-Mediated Dissociation of the C−C σ Bond in Acetone

Vanessa A. Castleberry, S. Jason Dee, Otsmar J. Villarroel, Ivanna E. Laboren, Sarah E. Frey, and Darrin J. Bellert*

Department of Chemistry and Biochemistry, Baylor University One Bear Place #97348, Waco, Texas 76798-7348

Received: May 15, 2009; Revised Manuscript Received: August 5, 2009

The time dependence of the gaseous unimolecular decomposition of the jet-cooled adduct ion, $Ni^+-OC(CH_3)_2$, was monitored through selective detection of the Ni^+CO fragment ion. Various resolved amounts of energy in the range 15600−18800 cm^{-1} were supplied to initiate the dissociation reaction through absorption of laser photons by the title molecular complex. First-order rate constants, $k(E)$, ranged from 113000 to 55000 s^{-1} and decreased with decreasing amounts of internal excitation. The energy used to initiate the reaction is well below that required to fragment C−C σ bonds and indicates the necessity of the Ni^+ cation to induce bond activation and fragmentation. These measurements are carried out in a unique apparatus and represent the first direct kinetic study of such catalytic type reactions.

Introduction

Gas phase atomic metal ions interact with organic molecules aggressively to cleave rather high energy bonds, essentially catalyzing these organometallic reactions. Often, a primary research objective is to understand the factors that facilitate the transition to bond activation. An expanding body of research[1−9] has been completed on this singular issue, which would indicate its potential impact. Thus, the energy lowering associated with metal-mediated bond activation within organic molecules is of obvious importance. A fundamental understanding of the energetic requirements, dynamics, and mechanism associated with metal-induced organic bond cleavage may be of practical significance to diverse fields such as enzymology[10−12] and to those industries researching and developing alternative energy sources.[13]

The body of literature associated with gas phase ion/molecule reactions is extensive and diverse.[14−22] We attempt to build upon this knowledge base through the direct experimental determination of the kinetics of ion/molecule reactions. Early ion cyclotron resonance[16] (ICR) studies firmly established ion/molecule reaction products and, under appropriate conditions, could speculate as to the mechanism and probable thermochemistry associated with the reaction. Freiser[16] and co-workers reacted Fe^+ with $(CD_3)_2CO$ and found the neutral reaction products to be 93% C_2D_6 and 7% CO. Collision induced dissociation (CID) studies often quantified the reaction thermochemistry and established bond energies of both reactants and products (and sometimes intermediates as well). Beauchamp and co-workers[19] measured the CID cross sections of the $Co^+ + (CH_3)_2CO$ reaction which established the exothermic production of C_2H_6 (90% yield) and CO (10% yield) + corresponding cations.

More recently, product kinetic energy release distributions (KERDs)[23−27] for ion/acetone reactions[28] have been measured. Here, the M^+−acetone adduct ions are formed hot in the source with sufficient internal energy to induce reaction. However, before complete unimolecular decomposition can occur, precursor ions are accelerated and mass isolated via transmission through a magnetic sector. Metastable ions then decompose in a second field free region. The kinetic energy distributed among the resulting product ions is the determining factor for transmission through a voltage tuned electric sector and, ultimately, detection. Bowers et al.[23] measured the KERD for the $CoCO^+$ product ion from the decomposition of $Co^+(CD_3)_2CO$. Their analysis indicated that C−C σ-bond activation was the rate-limiting step in the reaction coordinate. Furthermore, they reported the activation energy to be ∼43 kcal/mol (15000 cm^{-1}).

SCHEME 1

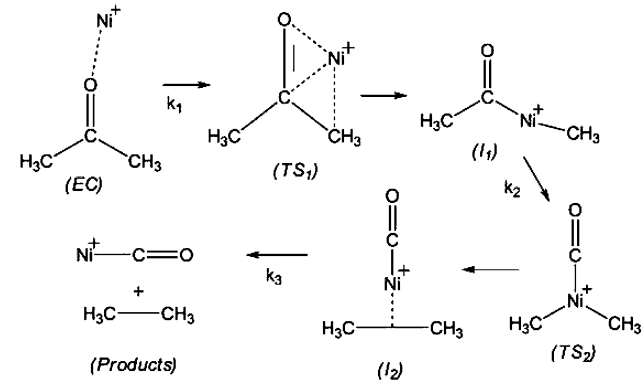

Recently, density functional theory (DFT)[29] has been applied to the $Ni^+ + Ac \rightarrow Ni^+CO + C_2H_6$ reaction. Scheme 1 is a simplified version of the reaction coordinate proposed by DFT calculations. It begins with the encounter complex (EC) which is the Ni^+ cation bound to the dipole moment of the acetone molecule. Once the EC receives sufficient energy to overcome an activation barrier, a multicentered Ni^+ transition state (TS_1) forms which leads to activation of a C−C σ bond. The Ni^+ inserted complex is labeled as the first intermediate (I_1) in Scheme 1. As the reaction progresses to products, the second intermediate forms (I_2) after transitioning through the three-bonded Ni^+ cation (TS_2). I_2 is a Ni^+CO molecule electrostatically bound to the ethane σ bond. The final step is breaking the electrostatic interaction and separation into products. This step

* Corresponding author, Darrin_Bellert@baylor.edu, fax 254-710-4272.

10.1021/jp904561y CCC: $40.75
Published on Web 09/03/2009

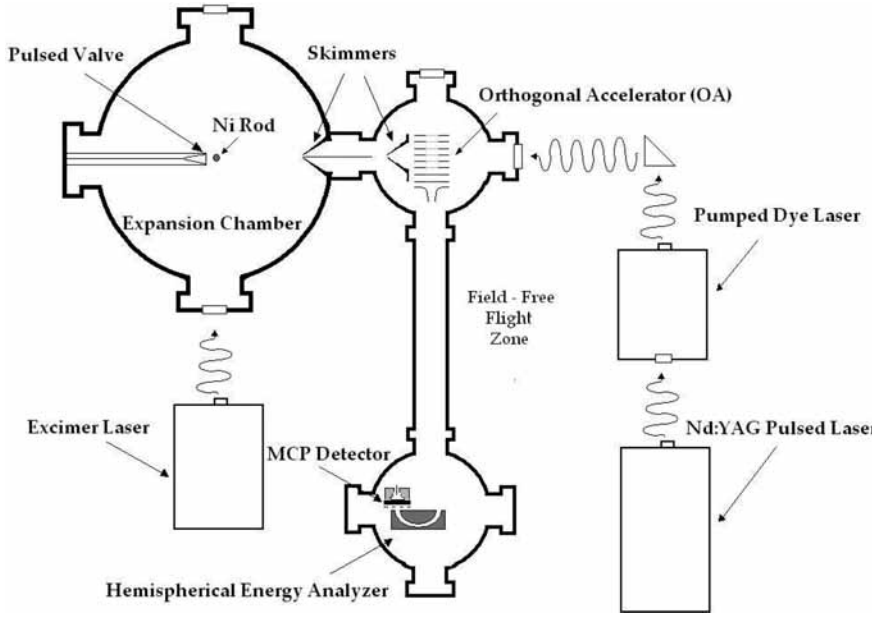

Figure 1. Instrumental diagram. Our apparatus consists of a large vacuum chamber coupled to a custom TOFMS. The TOF contains a pulsed orthogonal accelerator at the entrance and a kinetic energy analyzer at the terminus. The expanse between these two components represents the field free flight region where ionic fragment production is sampled.

occurs with minimal isomerization. According to these DFT calculations, the energy of TS_2 is greater than TS_1, indicating that the rate-limiting step is isomerization (CH_3 shift) rather than C−C σ-bond activation.

As indicated, our contribution to this science is the determination of unimolecular decomposition reaction rate constants. In a similar fashion as KERDs techniques, our experiment requires precursor ion dissociation to occur in the field free region of a time-of-flight mass spectrometer to produce detectable fragment ions. However, unique to this study is the formation of cold precursor ions, with minimal amounts of internal energy. The activation energy is supplied through absorption of a laser photon. The absorption is the initial step in the unimolecular dissociation reaction. The excited system then develops in time according to

$$A_t = A_0 e^{-kt} \quad (1)$$

The system presented here is the unimolecular decomposition of the Ni^+−acetone complex ion (Ni^+Ac) into $Ni^+CO + C_2H_6$ fragments, which is the only low energy path observed. In accord with Equation 1, the depletion of precursor Ni^+Ac ions is monitored as a function of time through selective detection of the charged Ni^+CO fragment. The rate constant k is then extracted from the decay waveform and represents the rate-limiting step (either formation of TS_1 or TS_2) along the reaction coordinate.

Experimental Section

(A) Instrumentation. In general, a large supersonic source chamber is connected to a custom time-of-flight mass spectrometer (TOFMS) as shown in Figure 1. Ionic clusters generated in the source are mass analyzed and detected in the TOF. Pulsed laser beams can be oriented to enter the vacuum apparatus through a variety of windows and the location of the laser entry dictates the type of experiment performed.

Specifically, the supersonic source chamber is a 120 L vacuum chamber (operational pressures $\sim 3 \times 10^{-6}$ Torr). An external motor couples motion into the vacuum chamber and rotates a $^1/_4$ in. nickel rod ($\sim$98% pure) at a rate of 1.1 rpm. The rotational motion is defined by high precision bearing rings press fit into an open configuration stainless steel source block. A high-pressure line is coupled into the vacuum chamber which connects to the source block through a series 9 General Valve. The valve/rod assembly is centrally located in this main vacuum chamber. Momentarily opening the solenoid valve allows high-pressure ($\sim$100 psi) helium gas, doped with the vapor pressure of liquid acetone, to supersonically expand into the vacuum chamber. As the expansion plume develops, 248 nm laser radiation from a pulsed KrF excimer is focused onto the rotating surface of the nickel rod, thus ablating the metal and seeding neutral and ionic nickel atoms into the jet-cooled expansion. The substantial number of collisions between the doped carrier gas and Ni^+ ensures the formation of the title Ni^+Ac complex. The large pressure drop (10^9) between the static gas reservoir and the vacuum chamber guarantees the formation of the title complex with minimal amounts of internal energy. Experimental conditions are optimized to produce the coldest ion beams possible (see below).

The expanding plume traverses $\sim$80 cm of field free space, is skimmed twice, and enters between parallel capacitor plates of a Wiley−McLaren[30] orthogonal accelerator (OA) located at the entrance of the TOFMS. The TOFMS is independently pumped and is maintained at an operational pressure of $\sim 2 \times 10^{-7}$ Torr. As the densest portion of the ion packet enters, the OA is pulsed from ground potential to +1.75 kV. The common kinetic energy imparted to the ions permits mass separation through the 1.8 m field free flight of the TOFMS. After the drift through field free space, the separated ion packets enter a voltage-controlled hemispherical kinetic energy analyzer (or sector). The sector is custom fabricated from 316 stainless steel and is supported within the TOFMS vacuum apparatus (it is bolted onto one of the flanges in the five cross). The entrance into the sector is located along the center line of the flight tube and naturally intersects the ion beam. The potential difference across the halves of the sector can be selected to transmit the full kinetic energy of the ion beam thus allowing the different

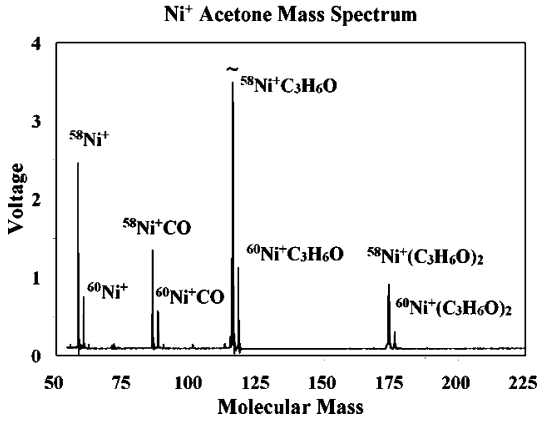

Figure 2. Characteristic precursor time-of-flight mass spectrum.

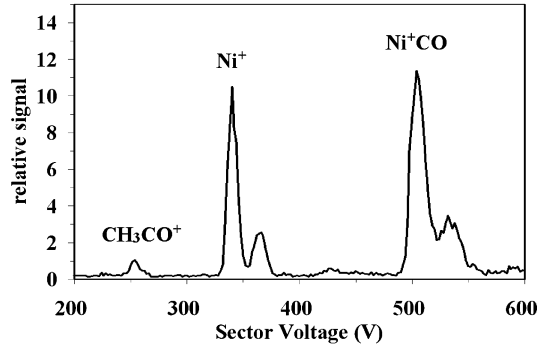

Figure 3. A sector scan. The *x*-axis represents the potential difference between the inner and outer surfaces of a hemispherical kinetic energy analyzer. The sector is voltage tuned while a pulsed laser (photon energy = 16400 cm^{-1}) induces dissociation of the precursor Ni^+Ac complex ion. The precursor ion dissociates into various charged fragments. These transmit through the sector at a characteristic potential difference. The identities of the fragment ions are indicated above the peaks, and the shoulders at higher voltage result from the $^{60}Ni^+$ isotope of each cluster.

ionic species produced in the expansion to strike a Chevron microchannel plate detector (Burle Industries) located at the sector's terminus. Precursor mass spectra (Figure 2) can then be acquired and analyzed to determine the identity and optimize the intensity of the complexes within the beam.

Laser-induced dissociation of a single precursor ion results in charged fragments that transmit through the sector at different characteristic voltage settings. Although the dissociation event does not significantly affect the fragment's velocity, the transmission voltage changes due to the change in mass of the fragment ion. Figure 3 shows such a fragment transmission profile resulting from the laser-induced dissociation of the Ni^+Ac precursor cluster ion. Here, 16400 cm^{-1} laser radiation is timed to intersect the Ni^+Ac precursor ion 6 μs before it enters the sector. The precursor ion dissociates into various charged fragments which transmit through the sector at their characteristic voltages. The three dissociative products which are observed in high yield are Ni^+, Ni^+CO, and CH_3CO^+. The shoulders observed in Figure 3 at ~365 and ~535 V are due to the ^{60}Ni isotope of each cluster.

Photodissociation studies, in which a pulsed laser field intersects the ion beam just before the ions enter the sector, reveal the various types of potential fragment ions at various laser energies. Although such preliminary experiments indicate the identity of possible fragment ions, probing the ion beam just in front of the sector proves incapable of measuring reaction rate constants. It is impossible to separate fragment ions created by a multiphoton absorption event from those generated through single photon absorption. In fact, each intense fragment ion peak, observed in Figure 3, is accentuated by multiphoton absorption.

Rather, to measure the unimolecular decay of a precursor ion, cations within the molecular beam absorb the photon energy prior to right angle extraction and mass separation within the TOF. This is accomplished by guiding the laser beam into the vacuum apparatus through a viewport counterpropagating to the supersonic expansion axis (this configuration is shown in Figure 1). The ionic molecules within the beam absorb the radiation and decay to produce fragment ions as the molecular beam approaches the OA. All fragment ions produced in the expanse between photon absorption and the OA receive the same (full) kinetic energy imparted to the precursor ions during right angle extraction. These "early" fragment ions are indistinguishable from the precursor beam and are therefore not detected. Only those precursor ions which decay within the field free flight of the TOF can be detected through selective transmission through the sector. Hence, our sector limits detection to those dissociation events which occur during precursor ion field free flight within the TOF. Decay curves are generated by a computer-controlled scan of the timing delays. The program varies when the dissociation laser encounters the molecular beam while measuring the intensity of selected fragment transmission through the sector. This is described in greater detail below.

Selectively monitoring fragment production which occurs only during the free flight time between the OA and sector discriminates against the detection of any fast dissociative events. Ions require ~2.4 μs to traverse the OA at nominal voltage settings, and any precursor which dissociates within the field of the OA will not be detected. Thus, fast two-photon dissociation processes provide minimal contamination to the fragment yield even at the high, pulsed laser fluences (30−50 mJ/pulse) employed for these studies.

Of the three fragment ion products observed in Figure 3, only production of Ni^+CO results from single-photon absorption. This has been confirmed by conducting the analogous sector scan but where the laser intersects the molecular beam 3 μs prior to orthogonal extraction. This effectively discriminates against dissociation caused by multiphoton absorption (which must be a comparatively fast process). The lack of observed signal indicates that the cleavage channel (production of Ni^+) and the charge transfer dissociative channel (production of CH_3CO^+) are multiphoton induced events. The only fragment ion resulting from single photon absorption is $NiCO^+$. Additionally, the identity of the fragment $NiCO^+$ has been confirmed through isotopic (deuterium) labeling of the acetone ligand. The transmission resolution of the sector is insufficient to separate Ni^+CO from $Ni^+C_2H_6$; however, the resolution is more than adequate to separate Ni^+CO from $Ni^+C_2D_6$ (which is not observed).

(B) Data Analysis. Molecular cations, upon absorption of the laser photon energy, will dissociate as indicated in Scheme 1. Because unimolecular decomposition is a first-order process, excited precursor ions will decay in accord with eq 1. This decomposition results in a characteristic decay curve for the molecule under a specific set of conditions. Regardless, this process is not what is measured directly in this study. Here, the precursor molecule absorbs radiation, thus initiating the reaction, before entering the OA. Only the precursors which decompose after exiting the OA, but prior to entering the sector, will produce detectable fragment ions. So, the molecular decay is sampled during the entire field free flight through the TOFMS. This sampling method has the effect of integrating eq 1 between two

well-defined limits: t_i = the time the precursor ions just exit the OA and t_f = the time just prior to the precursor ions entering the sector. The integrated area is then plotted as a single point, y_τ. The time τ represents the decay that is lost (not sampled) during the precursor ion's flight to the OA. Experimentally, the time τ equals the difference between the dissociation laser fire command and the pulse to trigger the OA. At zero τ, the laser intersects the ions within the OA, nanoseconds before the extraction pulse. Thus, the only fragment signals lost are from those precursors which decay within the 2.4 μs travel through the OA field. Zero τ will often represent a maximal point (most collected fragment signal) in the acquired decay curve. Positive values of τ represent the amount of time the precursors decay into undetectable fragments before right angle extraction, thus the measured signal decreases as τ increases. At negative τ values, the OA is triggered to fire before the dissociation laser and any collected signals observed result from a constant collision induced dissociative background.

The time, τ, equals t_i minus the precursor ions travel time through the OA (here, 2.4 μs). The signals acquired in this study result from integrating eq 1 between the limits t_i and t_f

$$y_\tau = A_0 \int_{t_i}^{t_f} e^{-kt}\, dt$$

$$= \frac{A_0}{k}(e^{-kt_i} - e^{-k(\Delta t + t_i)})$$

$$= \frac{A_0}{k}\left(e^{-kt_i}\left(1 - \frac{1}{e^{k\Delta t}}\right)\right) \quad (2)$$

where $\Delta t = t_f - t_i$ = the precursor ion's field free flight time (~38 μs) through the TOFMS.

Grouping the constants of eq 2 into α

$$\alpha = \frac{1 - \frac{1}{e^{k\Delta t}}}{k} \quad (3)$$

and substituting $t_i = \tau + 2.4$ μs results in eq 4, which has the same form of eq 1.

$$y_\tau = \left(\frac{\alpha}{e^{2.4k}}\right) A_0 e^{-k\tau} \quad (4)$$

Thus, a plot of y_τ vs τ should yield exponential decay as predicted by eq 1; however, this parenthetical term in eq 4 will often enhance the curve. Combining the α amplification with the rate constants observed in this study creates a data magnification of ~10−15 times. We have found our technique to be proficient at measuring first-order reaction rate constants in the range of ~0.6−0.01 μs^{-1}, and we believe this range likely extends from 1 to 0.005 μs^{-1}.

Results

(A) Initial Beam Conditions. Displayed in Table 1 are the energy specific reaction rate constants for the unimolecular decomposition of Ni^+Ac into $Ni^+CO + C_2H_6$. The internal energy of the ions is provided by absorption of the laser photon energy. As this energy is well-known, the resolution of the ion's internal energy is determined by the distribution of initial quantum states populated within the jet-cooled ion. Although there are multiple methods available to approximate the temperature of a supersonic expansion,[31,32] the characteristics of the beams typical to this study are approximated through fits of the ion velocity distribution within the expansion.

TABLE 1: First-Order Rate Constants Measured for the Unimolecular Decomposition Reaction: $Ni^+Ac \rightarrow Ni^+CO + C_2H_6$ at Various Internal Energies

internal energy (cm^{-1})	$k(E)$ (s^{-1})
18800	113000 ± 5000
18000	96800 ± 3000
17700	92700 ± 3000
16400	59000 ± 2000
16100	58000 ± 3000
15600	55000 ± 3000

It is widely accepted that collisions cool molecules expanding from a high-pressure source to an area of low pressure and that the expansion nozzle configuration will control the number of collisions.[33−38] Furthermore, collisions convert the internal energy (vibrational, rotational, and electronic degrees of freedom) of the gas molecules into directed mass flow. Moreover, as the expansion develops, the collision frequency drops to such low levels that no further cooling can occur. Under such collisionless conditions, assumptions of equilibrium are no longer valid and temperatures associated with the various modes of motion can be independently specified. The translational temperature can be defined in terms of the ion velocity distribution within the beam. In our studies, we define the ion velocity as the distance which the ions travel (~80 cm between the center of the OA and the nickel rod) relative to the difference in trigger pulses between the OA and excimer vaporization laser. This value is only an apparent velocity as no effort is made to determine the actual fire time of the pulsed equipment; however, this is of no consequence as the temperature is approximated from the distribution of ion velocities within the gas pulse and not the absolute velocities.

Figure 4 shows the normalized velocity distribution for the intense cluster ions seen in the mass spectrum of Figure 2. The distributions are simultaneously acquired by scanning the pulse triggering the OA while maintaining constant source conditions (e.g., excimer and pulse valve fire commands, excimer pulse

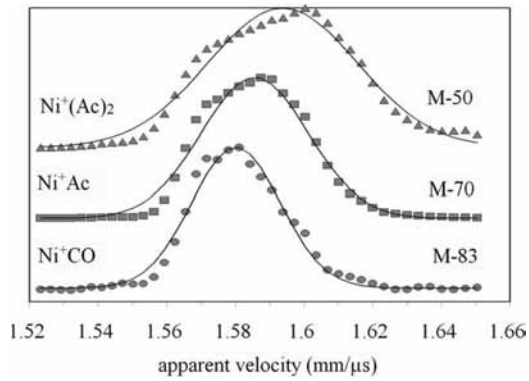

Figure 4. The apparent velocity distribution of the intense precursor clusters of Figure 2. Each trace represents a different precursor ion cluster. The three signals were acquired simultaneously while scanning the difference between the excimer laser trigger and the OA trigger. Thus, the peak width provides a measure of the velocity distribution within the molecular beam for each cluster ion. The solid line represents a fit of this distribution to eq 4, therefrom the translational temperature of the ions can be determined. The Mach values indicated above are calculated from the extracted temperature and eq 5.

fluence, etc.). Source conditions are optimized to produce the narrowest, most symmetric precursor ion velocity distribution.

The probability of a certain velocity (v) within the expansion can be derived from the Maxwell−Boltzmann distribution

$$P(v) = v^3 \exp\left(-\frac{m(v - \bar{u})^2}{2kT}\right) \quad (5)$$

where T is the local temperature,$\bar{u}$ is the average flow velocity in the expansion, and m is the weighted mass (95% He, 5% acetone) of the carrier gas. The translational temperature of the ions is determined by fitting eq 5 to the experimentally determined ion velocity distribution. The corresponding curves are shown as solid lines in Figure 4. These curves indicate the low ion translational temperatures within the beam. Those temperatures are less than 1 K for each precursor ion shown. The Mach number (M) is the ratio of the average flow velocity to the local speed of sound within the expanding gas and can be determined from the temperatures obtained from eq 5. The Mach numbers indicated in Figure 4 were calculated from eq 6,

$$M = \sqrt{\frac{2(T_r - T)}{T(\gamma - 1)}} \quad (6)$$

where T_r is the gas reservoir temperature (300 K) and γ is the ratio of the heat capacities for a 5/95 mixture of acetone vapor in helium.

The narrow velocity distributions and high Mach numbers evident in Figure 4 demonstrate the substantial cooling that occurs under optimal experimental conditions. Such high Mach numbers are not beyond the coldest supersonic expansions observed.[34] The traces of Figure 4 only indicate the translational temperature of the beam; however, it is the cooling of vibrational and rotational degrees of freedom that result in directed mass flow. Understandably, with 57 normal vibrational modes, $Ni^+(Ac)_2$ was not as effectively cooled in the supersonic expansion, resulting in a wider velocity distribution as compared to the other observed clusters. The coldest cluster ion in the beam is Ni^+CO, with only four vibrational modes storing internal energy. The velocity profile for the title molecular ion, Ni^+Ac, is only slightly larger than that observed for Ni^+CO. The minor increase would suggest that most of the vibrational energy has been removed. Therefore, perhaps only the lowest frequency vibrational modes of the cluster are populated at experimental conditions and these represent a negligible contribution to the internal energy of the ion.

Finally, there are two factors that help to cool ions relative to neutrals under supersonic expansion conditions and lead to the high Mach numbers observed here. (i) Ions seeded into the expansion plume suffer more cooling collisions relative to neutral molecules due to the long-ranged attractive potential (e.g., ion-dipole or ion-induced dipole), which occurs between the cation and acetone or helium. (ii) The presence of a positive charge bound to the dipole moment of acetone will tend to make the ionic cluster more rigid than the neutral. The added rigidity tends to raise the vibrational frequencies of the low energy vibrational motions of neutral acetone. The higher frequency modes are less likely to be populated at the reduced temperatures of the expansion.

(B) Reaction Rate Constants, $k(E)$. The lower panels of Figures 5−7 show the exponential decay profiles of Ni^+Ac dissociating into $Ni^+CO + C_2H_6$, which directly results from absorption of the laser photon energy. As the precursor cluster ions are jet-cooled in the supersonic expansion, the photon energy supplies the amount of internal energy available to the complex. The time axes of Figures 5−7 indicate when the pulsed laser is triggered to fire with respect to the ion's temporal displacement relative to the OA. The top traces of Figures 5−7 plot the natural logarithm of the integrated intensity as a function of time τ (eq 4). The linear portion of each decay profile was fit to a straight line and the rate constant ($k(E)$) was extracted

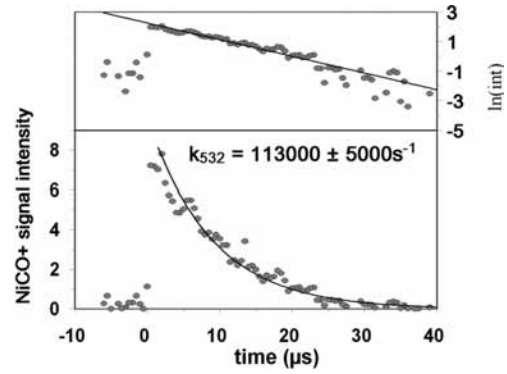

Figure 5. The bottom panel plots the intensity of acquired fragment (Ni^+CO) signal resulting from the precursor Ni^+Ac absorption of laser radiation (photon energy = 18800 cm^{-1}). The increasing time axis indicates when the dissociation laser is triggered to fire relative to the temporal displacement of the ions from the OA. Fewer dissociation events are detected at all positive values of time because a portion of the precursor decays into undetectable fragments before orthogonal extraction. This results in the first-order decay profile resulting from the unimolecular dissociative reaction of $Ni^+Ac \rightarrow Ni^+CO + C_2H_6$. The top panel plots the natural logarithm of the intensity vs time, thence the first-order rate constant is extracted. The rate constant is expressed in the figure and is labeled by the photon wavelength used to initiate the dissociation reaction.

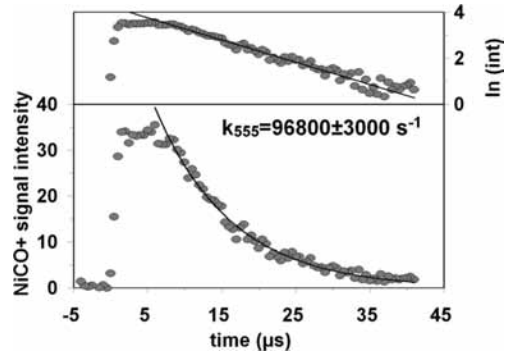

Figure 6. The same kinetic study as in Figure 5, except with a photon energy = 18000 cm^{-1}.

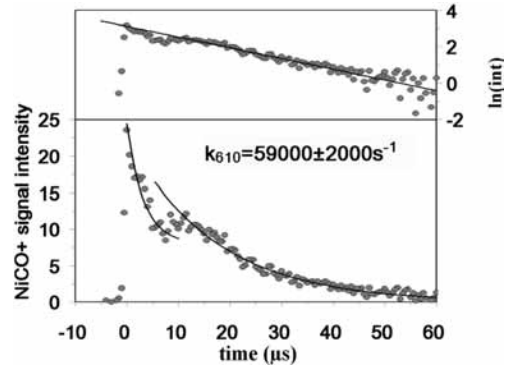

Figure 7. The same kinetic study as in Figure 5, except with a photon energy = 16400 cm^{-1}.

from linear regression analysis. The rate constants are provided in each figure as well as in Table 1 and clearly demonstrate dependence on the internal energy of the complex. As the internal energy of the complex decreases, so does the unimolecular dissociation rate constant.

The curves of Figures 5−7 show unique behavior at early times (0−12 μs) of the unimolecular decay. Figure 5 shows a decay profile fit adequately from 0−35 μsby a single rate constant, $k(E = 18800\ \text{cm}^{-1}) = 113000 \pm 5000\ \text{s}^{-1}$. In Figure 6, the early data (0−8 μs), does not vary with time, but follows first-order decay from 8 to 50 μs. From this portion of the curve, a single rate constant, $k(E = 18000\ \text{cm}^{-1}) = 96800 \pm 3000\ \text{s}^{-1}$ was extracted. Figure 7 shows a comparable decay profile. Here, the data acquired at long times (12−60 μs) show exponential decay described by a single rate constant $k(E = 16400\ \text{cm}^{-1}) = 59000 \pm 2000\ \text{s}^{-1}$. The early data appear to round off in a type of plateau, comparable to the observations in Figure 6; however, built on this time invariant portion of the profile is a fast decay curve with a relatively large rate constant. It is likely the fast decay component results from two-photon absorption, resulting in the significantly larger rate constant, ($k(E = 32800\ \text{cm}^{-1}) = 310000 \pm 40000\ \text{s}^{-1}$). The decay profiles of Figures 5−7 can be adequately described by assuming there are two rate constants that mediate the kinetics of the reaction. One of the rate constants is rate determining and the other is slightly larger, but both decrease with decreasing energy.

From Scheme 1, the likely choices for these two rate constants are k_1 (the formation of the multicentered Ni^+ transition state, TS_1) and k_2 (the formation of tricoordinated Ni^+, TS_2). The value of k_3 is assumed large as this involves the direct elimination of the electrostatically bound ethane molecule from Ni^+CO without rearrangement. This assumption is consistent with DFT calculation.[29] Scheme 1 suggests a reaction coordinate of consecutive steps to produce $Ni^+CO + C_2H_6$ from the precursor Ni^+Ac. Our data suggest the reaction kinetics is controlled by the formation of two transition states, making both k_1 and k_2 kinetically important steps along the reaction coordinate. The solutions to the differential rate equations that govern precursor loss and fragment production have been solved for this type of system by Harcourt and Esson.[39,40] Following their treatment, the time variations in the concentrations of $(Ni^+Ac)_t$, the first intermediate in Scheme 1 $(I_1)_t$, and product $(Ni^+CO)_t$ can be derived

$$(Ni^+Ac)_t = (Ni^+Ac)_0 e^{-k_1 t} \tag{7}$$

$$(I_1)_t = (Ni^+Ac)_0 \frac{k_1}{k_2 - k_1}(e^{-k_1 t} - e^{-k_2 t}) \tag{8}$$

$$(Ni^+CO)_t = \frac{(Ni^+Ac)_0}{k_2 - k_1}[k_2(1 - e^{-k_1 t}) - k_1(1 - e^{-k_2 t})] \tag{9}$$

we define the difference in rate constants as $\Delta k = |k_2 - k_1|$ Under conditions when Δk is large, eq 9 reduces to

$$(Ni^+CO)_t = (Ni^+Ac)_0(1 - e^{-\kappa t}) \tag{10}$$

where $\kappa = k_1$ when activation of the C−C σ bond is rate limiting ($k_1 \ll k_2$) and $\kappa = k_2$ when isomerization (the metal mediated methide shift) is rate limiting ($k_1 \gg k_2$). Regardless, under conditions when Δk is large, the production of fragment Ni^+CO occurs simultaneously as the precursor (k_1 rate limiting) or the intermediate (k_2 rate limiting) decays. This results in sharp behavior in the early times of the decay profile. Therefore, when the precursor Ni^+Ac contains 18800 cm^{-1} of internal energy, the dissociation kinetics is dominated by a single rate constant.

When Δk is small, a time lag between the initial decay of the precursor and the ultimate fragment formation may be observed. This time lag is referred to as an induction period. Such induction periods are common in radioactive, nuclear decay and result from either the relatively slow production and buildup of an intermediate or from the relatively slow consumption of the intermediate. These induction times, which become more apparent as Δk approaches zero, are responsible for the time-independent features in Figures 6 and 7. With 18000 cm^{-1} of internal energy, the induction time for the Ni^+Ac reaction forming products is ~10.4 μs(8 μs determined through inspection of Figure 6 plus the 2.4 μs travel time through the OA). Decreasing the amount of internal energy to 16400 cm^{-1} (Figure 7) results in an increased induction time to ~15 μs. The profile in Figure 5 appears sharp at 0 μs and decays continuously; thus the induction time associated with 18800 cm^{-1} of internal energy deposited into the Ni^+Ac ion is less than the travel time through the OA.

These results indicate that either formation of TS_1 and subsequent C−C σ-bond activation is rate limiting or the cation-mediated methyl migration is rate limiting. The induction period observed at photon energies below 18000 cm^{-1} is associated with the step that is not rate limiting. Since this technique is (currently) limited to the detection of only the final product Ni^+CO, we cannot confidently indicate which of the two processes is rate limiting and which results in the induction periods observed at low levels of internal energy. However, it is obvious that both the rate constants (k_1 and k_2) and the difference in the rate constants (Δk) decrease with decreasing amounts of internal energy.

Discussion

The ground electronic state bond energy of the Ni^+Ac complex ion has been calculated[29] as 20300 cm^{-1}, similar to the measured bond energy for the $Co^+(Ac)$ complex (18187 cm^{-1}).[23] The bonding is likely electrostatic as the ion-dipole attractive potential, determined at the $Ni^+-OC(CH_3)_2$ distance predicted by theory,[29] is 19600 cm^{-1}. The charge in the complex is localized on the nickel atom as justified by large difference in IP between the two bonding partners (the energy required to ionize atomic nickel is ~16500 cm^{-1} less than the energy required to ionize acetone[41]).

Upon laser irradiation, the Ni^+Ac complex ion absorbs a visible photon and is promoted to an electronically excited state. The Ni^+ cation must be the chromophore as electronic transitions in acetone occur only in the UV.[42,43] The lowest lying, excited electronic state of Ni^+ is a $^4F(3d^84s)$ with lowest energy spin−orbit component ($J = 9/2$) lying 8393.9 cm^{-1} above the Ni^+ ^2D ground state. Electronic transition to this ^4F manifold of states initiates the dissociative chemical reactions observed in this study. This Ni^+ centered electronic transition $\{^4F(3d^84s) \leftarrow {}^2D(3d^9)\}$ is both spin and parity forbidden. The prepared, excited quartet electronic state of Ni^+Ac is metastable; the absorbed photon energy is insufficient to cause direct dissociation into Ni^+ + acetone fragments (the energy of the prepared state is below the adiabatic bond energy of the complex) and coupling to the ground state through photon emission is optically forbidden. Rather, there are two probable fates for the metastable

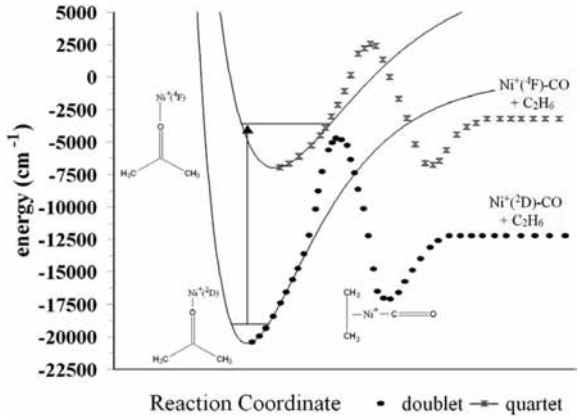

Figure 8. Semiquantitative Ni^+Ac potential energy surfaces (solid curve) superimposed upon a hypothetical $Ni^+Ac \rightarrow Ni^+CO + C_2H_6$ reaction coordinate (symbols). The potential energy surfaces are a slice along the $Ni^+-OC(CH_3)_2$ symmetric stretching coordinate and show both the ground doublet electronic state and excited quartet state. The vertical arrow indicates the type of electronic transition that initiates the dissociative reactions observed in this study. The symbols represent spin-specific reaction coordinates. They group any activated complex into a common maximum.

quartet state: (i) absorption of a second photon resulting in fast dissociation into fragments or (ii) intersystem crossing to the high vibrational levels of the ground, doublet electronic state. It is this latter process that provides the activation energy for the unimolecular dissociation of Ni^+Ac into $Ni^+CO + C_2H_6$ fragments.

Figure 8 shows qualitative potential energy surfaces for the purpose of demonstrating the deposition of energy into the ionic molecule. Both ground and excited state potentials represent a slice through the multidimensional surface along the $Ni^+-OC(CH_3)_2$ stretching coordinate. The well depth and bond length of the ground state surface were chosen to be consistent with DFT calculation.[29] The upper state bond was assumed to be 25% less bound and 15% longer than the ground state. This difference is consistent with the s ← d electronic promotion in Ni^+; electronic occupation of the s-orbital increases repulsions along the bond axis, and thus the excited state bond must be longer and weaker than the ground state. The energy difference at the Ni^+ + acetone separated limit is 8393.9 cm^{-1}, consistent with the electronic transition $\{^4F(3d^84s) \leftarrow {}^2D(3d^9)\}$ in atomic Ni^+. The potential energy surfaces of the ground and excited states of Ni^+Ac are superimposed upon oversimplified reaction coordinates (symbols of Figure 8). The doublet reaction coordinate (evolving from the doublet ground state) experiences an activation energy chosen to be consistent with experimental observation. The higher energy quartet reaction coordinate is a visual aid only. Neither doublet nor quartet reaction pathways will follow the symmetric $Ni^+-OC(CH_3)_2$ stretching coordinate. Rather, both break from the solid curve of Figure 8 at intermediate values of R_{Ni-O}. In the reaction coordinate (which may initially follow the $Ni^+-OC(CH_3)_2$ in plane bend), the Ni^+ migrates toward the C−C σ bond and activates the bond (via insertion) and the molecule isomerizes (a methide shift) and, finally, dissociates into products. A local minimum along the reaction path is the electrostatic, T-shaped Ni^+CO−ethane complex.

The vertical arrow of Figure 8 indicates the quartet ← doublet electronic transition, which occurs to initiate the Ni^+Ac decomposition reaction. The absorbed photon is at energies in excess of the activation energy along the doublet reaction coordinate. Fast intersystem crossing deposits the energy, supplied by the photon, into high lying vibrational states within the ground electronic state potential. Although internal vibrational redistribution (IVR) tends to scramble the energy into the various vibrational modes of the molecule, the cluster modes (those involving motion between the Ni^+ and the acetone molecule) are assumed to retain the bulk of the energy. This is conceivable since the Ni^+ cation is the chromophore in the transition (primarily $^4F(3d^84s) \leftarrow {}^2D(3d^9)$) and the cluster modes may inefficiently couple to the vibrational modes of the neutral. The net effect is the localization of energy and provision of sufficient motion between the Ni^+ cation and the acetone molecule to allow activation of the C−C σ bond. Again, it is only an assumption that inefficient IVR is at play. Ni^+CO is the only observed low-energy fragment and indicates that Ni^+ must move counter to the dipole moment of acetone prior to bond activation. This portion of the activation energy can be approximated from the DFT calculated reaction coordinate[29] as ~14000 cm^{-1}. It is unlikely that any fragment signal would be observed by this experimental technique if IVR efficiently channeled energy away from the reaction coordinate.

Once this inertial activation energy has been supplied, attractive forces between the Ni^+ cation and the carbon atoms within the organic permit completion of the reaction. It must be the electronic structure of the Ni^+ cation and the interactions along the reaction coordinate that account for bond activation and subsequent release of products. Bond energies of both the neutral (18300 cm^{-1}) and cationic (13900 cm^{-1}) Ni−CH_3 complexes have been calculated.[44] High level ab initio theory indicates the Ni^+CH_3 complex has one of the lowest M−C bond energies of the (n = 3) M^+CH_3 transition metal period. The neutral Ni−CH_3 analogue, however, has the highest M−C bond energy from this same period of M−CH_3 cluster molecules. According to calculations, the ion has more d character in the Ni−C bond relative to the neutral. Additionally, the bond energy of the Ni^+CO ion has been measured[17] at 14600 cm^{-1} and both ion and neutral are believed to have essentially identical bond energies.[44−46] To form I_2 (Scheme 1), the cation forms a covalent bond with each of the carbon atoms. Although the d^9 electronic configuration of Ni^+ is the most appropriate to activate the σ bond,[47] as the covalent bonds form, the cation likely promotes to the upper d^84s configuration, which now has two unpaired electrons capable of covalent bonding. The promotion energy is approximated as 8400 cm^{-1}. For Ni^+ to break the C−C σ bond of acetone, both the bond energy and Ni^+ promotion energy must be supplied, resulting in 38000 cm^{-1}. However, from this aliquot of energy, a portion is returned through Ni^+−C bond formation. Assuming the Ni^+CH_3 and Ni^+CO bond energies approximate this returned energy, the sum of these contributions place the intermediate roughly 9500 cm^{-1} above the Ni^+Ac global minimum. This value is 3300 cm^{-1} less than the DFT calculated predictions,[29] which placed the energy of I_1 12800 cm^{-1} in excess of the EC energy.

The final step in the mechanism is the formation of ethane resulting from a CH_3 shift across the Ni^+. The TS_2 (Scheme 1) has the Ni^+ bound to three carbon atoms. The electrostatic attraction between the slightly negative methyl group and the Ni^+ cation (and/or repulsions between the methyl group and the carbonyl oxygen) likely initiate the methyl shift to form the transition state. Moreover, to facilitate three bonds, the Ni^+ cation must again promote electrons (perhaps to empty p orbitals) or invoke hybridization; the energy cost is prohibitive. More likely, the Ni^+ cation returns to the initial d^9 configuration thus recovering the promotion energy and capitalizing on the electrostatic bonding with the three moieties. The loss of

s-character in the Ni^+-CH_3 bond would tend to weaken each Ni−C bond, which perhaps directs the formation of the product ethane. The re-formation of the σ bond (in ethane) recovers the initial energy input required to break the C−C bond of acetone, and the final intermediate is the Ni^+CO complex electrostatically bound to a neutral ethane molecule. Release of ethane follows allowing detection of the separated Ni^+CO fragment. Therefore, Ni^+ may exhibit the subtle interplay between ionic and partially covalent (s−d promotion) bonding character, which allows activation of reactants and subsequent release of products.

Conclusions

The kinetics associated with the unimolecular decomposition reaction: $Ni^+Ac \rightarrow Ni^+CO + C_2H_6$ has been studied in unique fashion over a range of internal energies. The energies employed in this study are below the adiabatic bond energy of the complex and well below the energy required to dissociate a C−C σ bond in an isolated organic molecule. The decay waveforms acquired here at low internal energies are composed of an induction period followed by first-order decay. These findings indicate the reaction kinetics are controlled by the formation of two transition states at low internal energies. One of these two processes is associated with the induction time in the decay waveform while the other is the rate-determining step in the dissociative reaction. Rate constants between 113000 ± 5000 and $55000 \pm 3000\ s^{-1}$ were determined from the experimental data between 18800 and 15600 cm^{-1}, respectively. As decreasing amounts of internal energy were supplied to the complex, the rate constants decreased, accordingly.

Although this type of reaction has been studied extensively, our findings represent the first experimental determination of the kinetics of this type of reaction. Continued research in this area not only will allow the determination of rate constants but also will shed light on the dynamics associated with this and similar "catalytic-type" reactions.

Acknowledgment. We gratefully acknowledge research support from the ACS Petroleum Research Fund (44393-G6). Additionally, funds from the Baylor University Research Committee and the Vice Provost for Research supported this study.

References and Notes

(1) Allison, J. In *Progress in Inorganic Chemistry*; Lippard, S. J., Ed.; Wiley: New York, 1986; Vol. 34.
(2) Beauchamp, J. L.; Van Koppen, P. A. M. *NATO ASI Ser., Ser. C* **1992**, *367*, 287.
(3) Hettich, R. L.; Freiser, B. S. Gas-Phase Photodissociation of Transition Metal Ion Complexes and Clusters In *Fourier Transform Mass Spectrometry*; Buchanan, M. V., Ed.; ACS Symposium Series 359; American Chemical Society: Washington, DC, 1987.
(4) Buckner, S. W.; Freiser, B. S. In *Gas Phase Inorganic Chemistry*; Russell, D. H., Ed.; Plenum Press: New York, 1989.
(5) Dunbar, R. C. In *Gas Phase Inorganic Chemistry*; Russell, D. H., Ed.; Plenum Press: New York, 1989.
(6) Weisshaar, J. C. In *Gas-Phase Metal Reactions*; Fontijn, A., Ed.; Elsevier: Amsterdam, 1992.
(7) Operti, L.; Rabezzana, R. *Mass Spectrom. Rev.* **2006**, *25*, 483.
(8) Freiser, B. S. *J. Mass Spectrom.* **1996**, *31*, 703.
(9) Mo, O.; Yanez, M.; Salpin, J-.Y.; Tortajada, J. *Mass Spectrom. Rev.* **2007**, *26*, 474.
(10) Cabri, W. *Catal. Today* **2009**, *140*, 2.
(11) Pordea, A.; Ward, T. R. *Chem. Commun.* **2008**, *36*, 4239.
(12) Yang, N.; Reiher, M.; Wang, M.; Harmer, J.; Duin, E. C. *J. Am. Chem. Soc.* **2007**, *129*, 11028.
(13) Wong, W.-Y. *Macromol. Chem. Phys.* **2008**, *209*, 14.
(14) Hettich, R. L.; Freiser, B. S. *Organometallics* **1989**, *8*, 2447.
(15) Surjasasmita, P. I.; Freiser, B. S. *J. Am. Soc. Mass Spectrom.* **1993**, *4*, 135.
(16) Burnier, R. C.; Byrd, G. D.; Freiser, B. S. *J. Am. Chem. Soc.* **1981**, *103*, 4360.
(17) Khan, F. A.; Steele, D. L.; Armentrout, P. B. *J. Phys. Chem.* **1995**, *99*, 7819.
(18) Liu, F.; Zhang, X. G.; Armentrout, P. B. *Phys. Chem. Chem. Phys.* **2005**, *7*, 1054.
(19) Halle, L. F.; Crowe, W. E.; Armentrout, P. B.; Beauchamp, J. L. *Organometallics* **1984**, *3*, 1694.
(20) Halle, L. F.; Armentrout, P. B.; Beauchamp, J. L. *Organometallics* **1982**, *1*, 963.
(21) Elkind, J. L.; Armentrout, P. B. *J. Phys. Chem.* **1986**, *90*, 6576.
(22) Baer, T.; Hase, W. L. *Unimolecular Reaction Dynamics: Theory and Experiments*; Oxford University Press: New York, 1996.
(23) Carpenter, C. J.; van Koppen, P. A. M.; Bowers, M. T. *J. Am. Chem. Soc.* **1995**, *117*, 10976.
(24) Laskin, J.; Lifshitz, C. *J. Mass Spectrom.* **2001**, *36*, 459.
(25) Hanratty, M. A.; Beauchamp, J. L.; Illies, A. J.; van Koppen, P. A. M.; Bowers, M. T. *J. Am. Chem. Soc.* **1988**, *110*, 1.
(26) Van Koppen, P. A. M.; Bowers, M. T.; Fisher, E. R.; Armentrout, P. B. *J. Am. Chem. Soc.* **1994**, *116*, 3780.
(27) Van Koppen, P. A. M.; Brodbelt Lustig, J.; Bowers, M. T.; Dearden, D. V.; Beauchamp, J. L.; Fisher, E. R.; Armentrout, P. B. *J. Am. Chem. Soc.* **1991**, *113*, 2359.
(28) Yi, S. S.; Reichart, E. L.; Weisshaar, J. C. *Int. J. Mass Spectrom.* **1999**, *185/186/187*, 837.
(29) Chen, X.; Guo, W.; Zhao, L.; Fu, Q. *Chem. Phys. Lett.* **2006**, *432*, 27.
(30) Wiley, W. C.; McLaren, I. H. *Rev. Sci. Instrum.* **1955**, *26*, 1150.
(31) Mayer, P. M.; Baer, T. *Int. J. Mass Spectrom. Ion Processes* **1996**, *156*, 133.
(32) Weitzel, K. M.; Booze, J. A.; Baer, T. *Chem. Phys.* **1991**, *150*, 263.
(33) Morse, M. D. *Exp. Methods Phys. Sci.* **1996**, *29B*, 21.
(34) Levy, D. H. *Annu. Rev. Phys. Chem.* **1980**, *31*, 197.
(35) Anderson, J. B. In *Molecular Beams and Low Density Gasdynamics*; Wegener, P. P., Ed.; Marcel Dekker: New York, 1974.
(36) Smalley, R. A.; Wharton, L.; Levy, D. H. *Acc. Chem. Res.* **1977**, *10*, 139.
(37) Miller, J. C.; Compton, R. N. *J. Chem. Phys.* **1986**, *84*, 675.
(38) Levy, D. H. *Science* **1981**, *214*, 263.
(39) Laidler, K. J. *Chemical Kinetics*, 3rd ed.; Harper and Row: New York, 1987.
(40) Harcourt, A. V.; Esson, W. *Proc. R. Soc. London* **1865**, *14*, 470.
(41) Shimanouchi, T., *Tables of Molecular Vibrational Frequencies Consolidated Volume I*; National Bureau of Standards: Washington, DC, 1972; pp 1−160.
(42) Haas, Y. *Photochem. Photobiol. Sci.* **2004**, *3*, 6.
(43) Goncharov, V.; Herath, N.; Suits, A. G. *J. Phys. Chem. A* **2008**, *112*, 9423.
(44) Bauschlicher, C. W., Jr.; Langhoff, S. R.; Partridge, H.; Barnes, L. A. *J. Chem. Phys.* **1989**, *91*, 2399.
(45) Barnes, L. A.; Rosi, M.; Bauschlicher, C. W., Jr. *J. Chem. Phys.* **1990**, *93*, 609.
(46) Blomberg, M.; Brandemark, U.; Johansson, J.; Siegbahn, P.; Wennerberg, J. *J. Chem. Phys.* **1988**, *88*, 4324.
(47) Armentrout, P. B. *Science* **1991**, *251*, 175.

JP904561Y